

Lawrence Berkeley National Laboratory

LBL Publications

Title

Observation of dimension-crossover of a tunable 1D Dirac fermion in topological semimetal NbSixTe2

Permalink

<https://escholarship.org/uc/item/03d7k55n>

Journal

npj Quantum Materials, 7(1)

ISSN

2397-4648

Authors

Zhang, Jing

Lv, Yangyang

Feng, Xiaolong

et al.

Publication Date

2022

DOI

10.1038/s41535-022-00462-6

Peer reviewed

ARTICLE OPEN



Observation of dimension-crossover of a tunable 1D Dirac fermion in topological semimetal NbSi_xTe_2

Jing Zhang^{1,2}, Yangyang Lv³, Xiaolong Feng⁴, Aiji Liang^{1,5}, Wei Xia^{1,5}, Sung-Kwan Mo⁶, Cheng Chen^{1,6,7}, Jiamin Xue¹, Shengyuan A. Yang⁴, Lexian Yang⁸, Yanfeng Guo^{1,5}, Yanbin Chen³, Yulin Chen^{1,5,7}✉ and Zhongkai Liu^{1,5}✉

Condensed matter systems in low dimensions exhibit emergent physics that does not exist in three dimensions. When electrons are confined to one dimension (1D), some significant electronic states appear, such as charge density wave, spin-charge separations, and Su-Schrieffer-Heeger (SSH) topological state. However, a clear understanding of how the 1D electronic properties connects with topology is currently lacking. Here we systematically investigated the characteristic 1D Dirac fermion electronic structure originated from the metallic NbTe_2 chains on the surface of the composition-tunable layered compound NbSi_xTe_2 ($x = 0.40$ and 0.43) using angle-resolved photoemission spectroscopy. We found the Dirac fermion forms a Dirac nodal line structure protected by the combined \bar{M}_y and time-reversal symmetry T and proves the NbSi_xTe_2 system as a topological semimetal, in consistent with the ab-initio calculations. As x decreases, the interaction between adjacent NbTe_2 chains increases and Dirac fermion goes through a dimension-crossover from 1D to 2D, as evidenced by the variation of its Fermi surface and Fermi velocity across the Brillouin zone in consistence with a Dirac SSH model. Our findings demonstrate a tunable 1D Dirac electron system, which offers a versatile platform for the exploration of intriguing 1D physics and device applications.

npj Quantum Materials (2022)7:54; <https://doi.org/10.1038/s41535-022-00462-6>

INTRODUCTION

Low dimensional electronic states bear fascinating emergent physics and have attracted great research interests in the past decade. For example, some of the two-dimensional (2D) electronic states under intensive investigation include electronic structure of van der Waals (vdW) materials in the atomic limit^{1–7}, the quantum well states confined on the surface/interfaces of semiconductors^{1,8,9} and topological surface states of strong topological insulators^{10–13}. They host profound physics including Ising superconductivity^{14–16}, charge density wave^{17–20}, spin-momentum locking^{21,22}, and magnetism^{23–25}. As electrons are confined into a one-dimensional (1D) wire, fundamentally important phenomena may emerge, such as Peierls phase transition (Peierls instability)^{26,27}, Su-Schrieffer-Heeger (SSH) topological state²⁸ and solitonic excitation^{29–31}, topological edge^{32–34}/hinge^{35–37} states, as well as Tomonaga-Luttinger liquid behavior^{38–40} due to electron correlation. These meaningful properties, together with the topological protection due to the bulk-surface correspondence in topologically nontrivial quantum materials, making low dimensional electronic states candidates for next-generation electronic devices.

Despite these great interests, the experimental realization of a tunable 1D electronic states appears to be rare. Physical systems with 1D electron systems include the self-assembly growth of metal wires on semiconductor surface (e.g., In^{41} , $\text{Ge}^{42,43}$, Si^{44} , GaN^{45} wires on $\text{Si}(111)$, Au wires on $\text{Ge}(110)^{46}$ and $\text{Ge}(001)^{47}$, $\text{MoO}_x^{48,49}$, $\text{Li}_{0.9}\text{Mo}_6\text{O}_{17}^{50}$, $\text{Rb}_{0.3}\text{MoO}_3^{51}$, TaSe_3^{52} , XTe_3 ($X = \text{Nb}, \text{V}, \text{Ti}$)⁵³, NbSe_3^{54} , etc. However, a few of them can be served as a stoichiometric compounds system for research on tunable 1D

electronic states^{55–57}. For the ease of investigation, manipulation and device fabrication, it would be desirable to search for stoichiometric compounds hosting tunable 1D electronic states.

Recently, the family of composition-tunable compounds NbSi_xTe_2 ($x = 0.33$ to 0.5) or $\text{Nb}_{2n+1}\text{Si}_n\text{Te}_{4n+2}$ ($n = 1, 2, \dots, \infty$) offers an ideal platform for studying 1D electrons. Previous studies have revealed 1D metallic NbTe_2 chain structure^{58,59}, 1D unidirectional massless Dirac fermions ($x = 0.45$)⁶⁰ and nodal line structure protected by the nonsymmorphic glide mirror symmetry ($x = 0.33$)^{61,62}. By changing n or x values, the spacing between neighboring chains could be altered, which results in the tunable electronic states⁶³. The gapless nature, fast electron velocity ($\sim 10^5 \text{ m s}^{-1}$), great tunability as well as thermal and air stability will facilitate its future applications in 1D electronics. However, the 1D nature of the Dirac fermion, its relationship with topology, as well as its evolution with different x values, has not been systematically investigated and carefully explained.

In this work, by using angle-resolved photoemission spectroscopy (ARPES), we systematically studied the electronic structure of NbSi_xTe_2 with varying x values. Our result proves the 1D nature of the characteristic Dirac fermion, which forms a nodal line structure along the Brillouin zone (BZ) boundary protected by the nonsymmorphic symmetry, showing a good agreement with the ab-initio calculations. Interestingly, in samples with smaller x , the 1D Dirac fermion experiences a dimension-crossover from 1D to 2D as evidenced by the enhanced variation in the Fermi surface and the Dirac fermion velocity across the nodal line. Such dimension-crossover is due to the stronger interactions between the neighboring metallic NbTe_2 chains, which could be nicely

¹School of Physical Science and Technology, ShanghaiTech University, 201210 Shanghai, China. ²University of Chinese Academy of Sciences, 100049 Beijing, China. ³National Laboratory of Solid-State Microstructures, School of Physics and Collaborative Innovation Centre of Advanced Microstructures, Nanjing University 210093 Nanjing, China. ⁴Research Laboratory for Quantum Materials, Singapore University of Technology and Design, Singapore 487372, Singapore. ⁵ShanghaiTech Laboratory for Topological Physics, 201210 Shanghai, China. ⁶Advanced Light Source, Lawrence Berkeley National Laboratory, Berkeley, CA 94720, USA. ⁷Department of Physics, University of Oxford, Oxford OX1 3PU, UK. ⁸State Key Laboratory of Low Dimensional Quantum Physics, Department of Physics, Tsinghua University, 100084 Beijing, China.

✉email: yulin.chen@physics.ox.ac.uk; liuzhk@shanghaitech.edu.cn

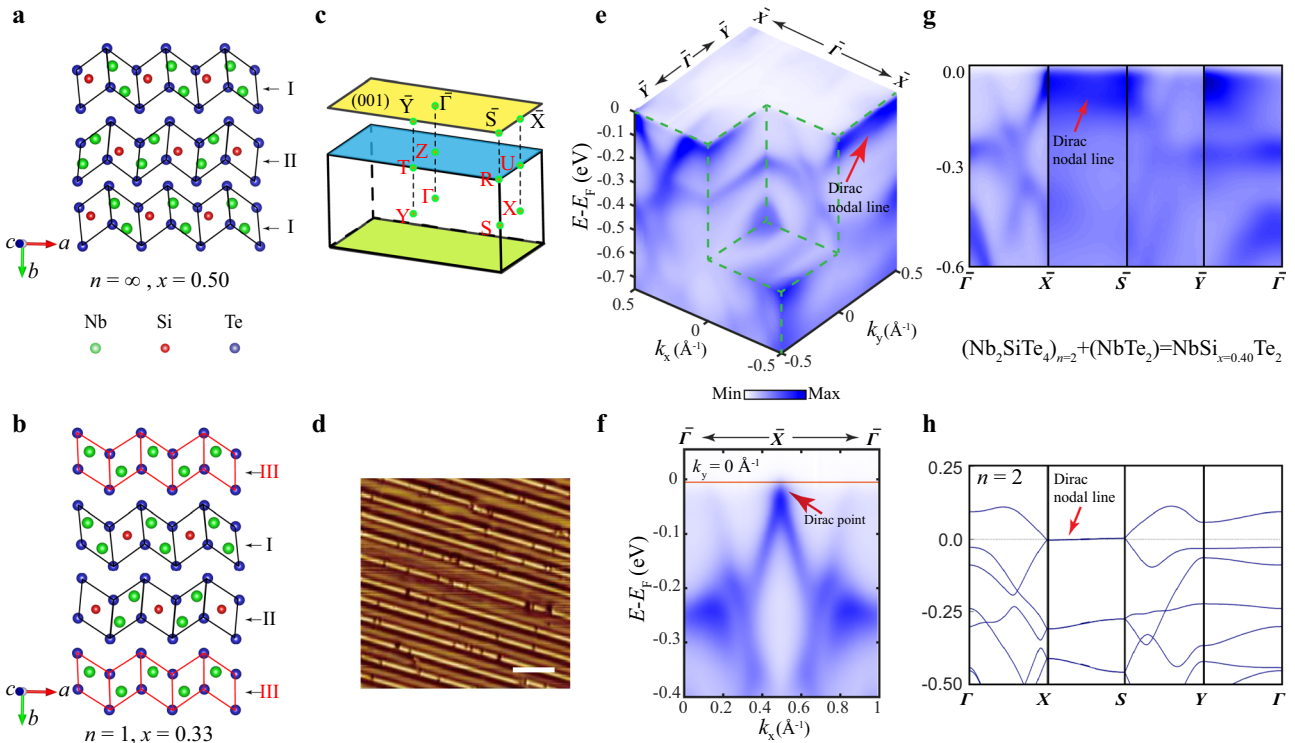


Fig. 1 Crystal structure and characterizations of NbSi_xTe_2 . **a** Crystal structure of Nb_2SiTe_4 ($n = \infty$, $x = 0.5$). Type I and II are two kinds of chains along the a -axis as building blocks. **b** Crystal structure of Nb_3SiTe_6 ($n = 1$, $x = 0.33$). Type I, II and III are three kinds of chains as building blocks. **c** The Brillouin zone (BZ) and its projection to the (001) surface of Nb_3SiTe_6 . **d** STM topography image of NbSi_xTe_2 . The bright lines show the metallic NbTe_2 chain (type III). Scale bar represents 10 nm. **e** 3D volume plot of the overall band structure of $x = 0.40$ ($n = 2$) sample with Dirac nodal line labeled. **f** The photoemission spectrum along the high symmetry $\bar{\Gamma} - \bar{X} - \bar{\Gamma}$ directions of $x = 0.40$ ($n = 2$) sample. Dirac point (DP) is labeled on the spectrum. **g** The photoemission spectrum along the high symmetry $\bar{\Gamma} - \bar{X} - \bar{S} - \bar{Y} - \bar{\Gamma}$ direction of $x = 0.40$ ($n = 2$) sample. Dirac nodal line is labeled. **h** The ab-initio calculated band structure of $x = 0.40$ ($n = 2$) sample from ref. 63. Dirac nodal line is labeled. Data in Fig. 1e–g were collected at $h\nu = 56$ eV with sample temperature 20 K. For STM topography measurement, the bias voltage is 0.7 V, and the tunneling current is 50 pA. The sample temperature is 4.2 K. Data from ref. 58 (Reprinted (adapted) with permission from ref. 58. Copyright (2022) American Chemical Society).

captured by our proposed Dirac SSH model that incorporates the important nonsymmorphic symmetry constraint into the conventional SSH model. Our observation demonstrates a tunable 1D Dirac fermion that could be utilized in device applications such as fast unidirectional conduction wires.

RESULTS

Crystal structure and characterizations of NbSi_xTe_2

The NbSi_xTe_2 are vdW crystals with layered structures. Each layer is constituted of three kinds of chain-like structures as building blocks (Fig. 1a, b): type I and II are semiconducting Nb_2SiTe_4 chains and type III are metallic NbTe_2 chains. With the inclusion of the NbTe_2 chains, NbSi_xTe_2 or $\text{Nb}_{2n+1}\text{Si}_n\text{Te}_{4n+2}$ becomes metallic. With different n or x values, the lattice structure also changes from the orthorhombic lattice (space group $Pnma$, No. 62) with $x = 0.33$ ($n = 1$) to the monoclinic lattice (space group $P12_1/c1$, No. 14) with $x = 0.50$ ($n = \infty$), but the non-symmorphic glide mirror symmetry \tilde{M}_y perpendicular to the b -axis is preserved. The BZ of $x = 0.33$ ($n = 1$) is shown in Fig. 1c. And STM topography image of NbSi_xTe_2 clearly indicates the existence of the metallic chains, which are shown in form of bright lines in Fig. 1d (data from ref. 58).

The representative electronic bandstructure of $x = 0.40$ ($n = 2$) sample could be found in Fig. 1e–g. Dispersions across the Fermi level are observed, suggesting its metallic nature. We note a linear dispersion could be found along the $\bar{\Gamma} - \bar{X} - \bar{\Gamma}$ direction (Fig. 1f) and the Dirac point forms a flat band along the $\bar{X} - \bar{S}$ direction (Fig. 1g), indicating a Dirac nodal line structure protected by the

combined \tilde{M}_y and time-reversal symmetry T . Our measurement shows nice agreement with the ab-initio calculations (Fig. 1h, also see ref. 63) (The spin-orbit coupling effect in this system is fairly weak and only leads to very small band splitting thus could be neglected^{61,63}, see discussion in Supplementary Fig. 1).

Band structure of the 1D Dirac fermion of $x = 0.43$ ($n = 3$) sample

We proved the 1D Dirac fermions nature by measuring its dispersion and evolution along all momentum directions (see the schematic of 1D Dirac fermion in Fig. 2b, c). The Dirac cone shape is pronounced along the $\bar{\Gamma} - \bar{X} - \bar{\Gamma}$ (k_x) direction, as could be observed in the second derivative of the spectrum of $x = 0.43$ ($n = 3$) sample (Fig. 2a). The estimated Fermi velocity is 1.07 eV Å ($\sim 1.63 \times 10^5$ m s⁻¹). Along the X - S (k_y) and X - U (k_z) directions, the Dirac fermion does not show significant change, as evidenced by the constant energy contour of E_F in the $k_x - k_y$ (Fig. 2d) and $k_x - k_z$ plane (Fig. 2f), as well as the evolution of the Dirac fermion dispersion measured at different k_y values (Fig. 2e) and different photon energies (Fig. 2g). The clear dispersion along k_x direction and dispersionless behavior along k_y and k_z directions demonstrate the 1D Dirac fermion behavior.

Dimension-crossover of the Dirac fermion

Profoundly, we observed the shape of the 1D Dirac fermion shows obvious change with the silicon deficiency x (the x level is confirmed by BZ size measured from ARPES as well as the STM

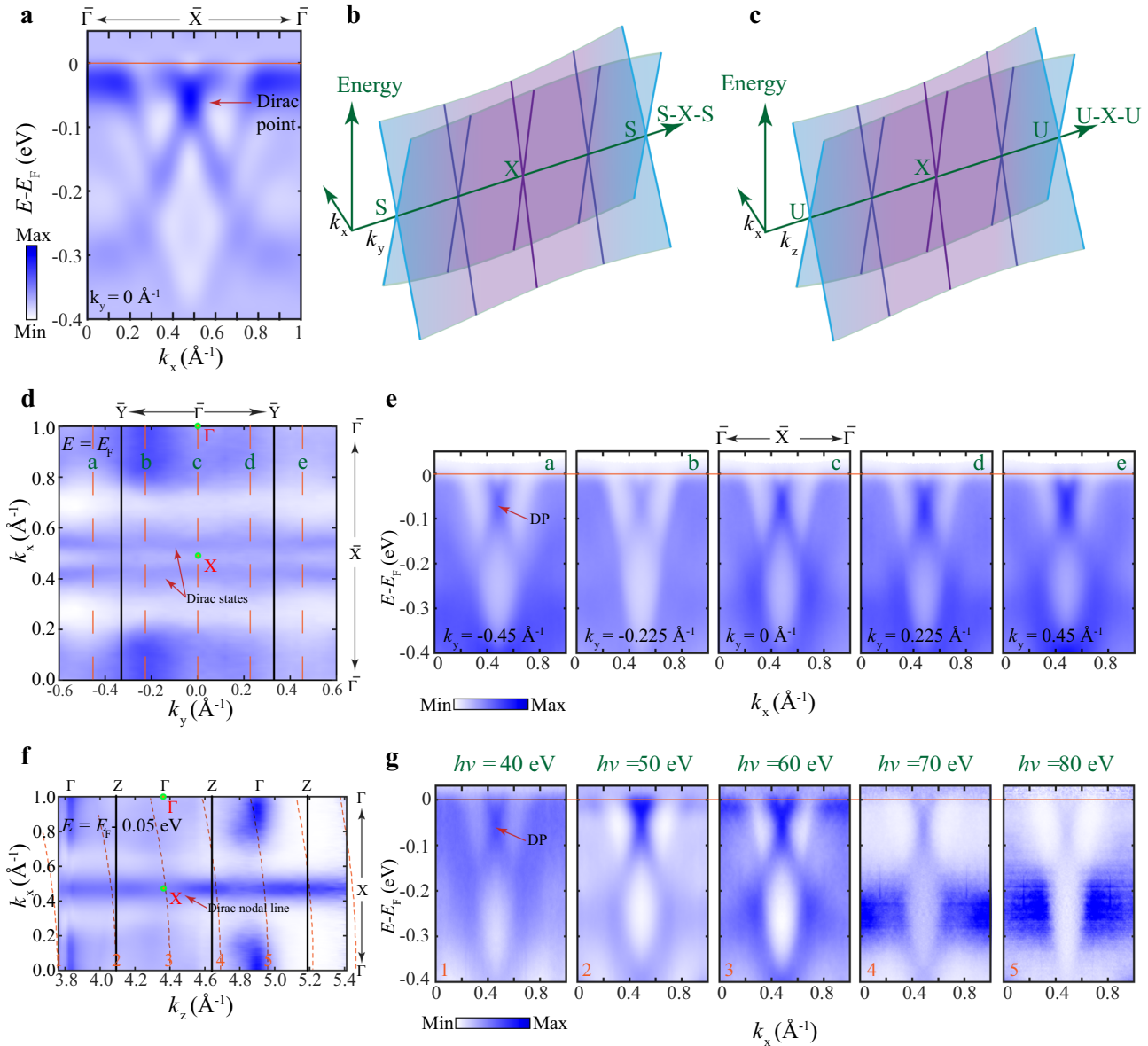


Fig. 2 Band structure of the 1D Dirac fermion of $x = 0.43$ ($n = 3$) sample. **a** Second derivative of the photoemission spectrum $\frac{d^2A}{d\omega^2}$ along $\bar{\Gamma} - \bar{X} - \bar{\Gamma}$ with DP labeled. **b, c** Schematic of the 1D Dirac fermion along the S-X-S (k_y) and U-X-U (k_z) directions. **d** The constant energy contour at Fermi energy (E_F) in the $k_x - k_y$ plane with Dirac surface states labeled and theoretical BZ appended (black solid lines). **e** Sliced cut in Fig. 2d at different k_y (orange dashed lines indicated in 2d) with DP labeled. **f** The energy contour near Fermi energy (E_F) of the $k_x - k_z$ plane with Dirac nodal line labeled. **g** Sliced cuts in Fig. 2f at different $h\nu$ (k_z - orange dashed lines) with DP labeled. To make a clear comparison, we symmetrized the dispersion according to the crystal symmetry. The data in Fig. 2a, d were collected at $h\nu = 55$ eV.

results, see Supplementary Fig. 3). As the x value is reduced (n is increased), the metallic NbTe₂ chains are aligned closer and start to interact with each other by increasing the overlap between the electron wavefunctions from adjacent chains (e.g. the average distance between NbTe₂ chains in samples with $x = 0.43$ ($n = 3$)/ $x = 0.33$ ($n = 1$) are 27.7 Å/12.1 Å, respectively, see Fig. 3a, b). Previous STM results report such phenomenon with metallic chain distance varies with different x values⁶³ (also see Fig. 1d). The interchain coupling allows electrons to hop between chains and drives the 1D to 2D dimension-crossover (see schematic in Fig. 3c, d). Such dimension-crossover is clearly demonstrated in the constant energy contour near E_F which shows the Dirac cone feature as two parallel lines for $x = 0.43$ ($n = 3$) samples (Fig. 3e), and alternating shapes (rounded circle to thin line) from the \bar{S} to \bar{X} points for $x = 0.40$ ($n = 2$) samples (Fig. 3h). The evolution of the

Dirac cone dispersion along the k_y direction could be found in Fig. 3e-j. As for $x = 0.43$ ($n = 3$) sample, the Dirac velocity is 1.07 eV Å ($\sim 1.63 \times 10^5$ m s⁻¹) along $\bar{\Gamma} - \bar{X} - \bar{\Gamma}$ (Fig. 3f) and 0.98 eV Å ($\sim 1.49 \times 10^5$ m s⁻¹) at $k_y = -0.30$ Å⁻¹ (Fig. 3g); while for $x = 0.40$ ($n = 2$) sample, the Dirac velocity is 1.44 eV Å ($\sim 2.19 \times 10^5$ m s⁻¹) along $\bar{\Gamma} - \bar{X} - \bar{\Gamma}$ (Fig. 3i) and 0.81 eV Å ($\sim 1.23 \times 10^5$ m s⁻¹) at $k_y = 0.30$ Å⁻¹ (Fig. 3j). The rapid change of Dirac velocity is consistent with the schematic in Fig. 3c, d and suggests the 1D to 2D crossover of the Dirac fermions observed.

Dimension-crossover and the Dirac SSH model of the Dirac fermion

The Dirac velocity evolution across the BZ of the two x ratio samples are summarized in Fig. 4a (Dirac velocity evolution of other x ratios is shown in Supplementary Fig. 5). Clearly, we could

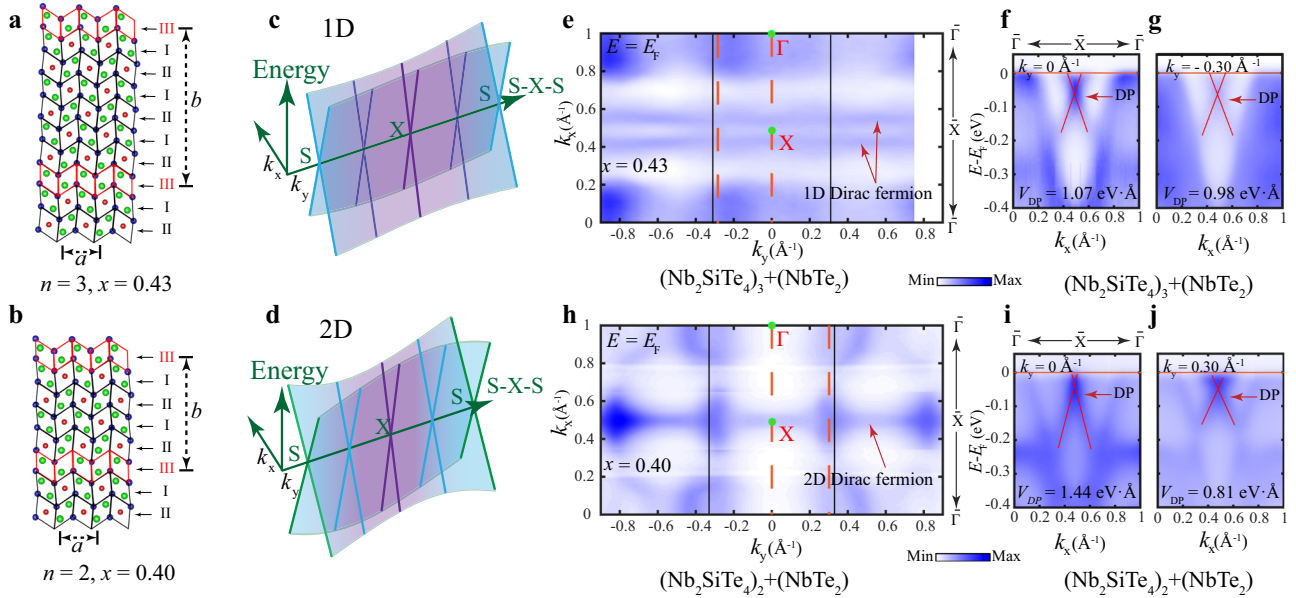


Fig. 3 Dimension-crossover of the Dirac fermion. **a, b** Crystal structure of **(a)** $x = 0.43$ ($n = 3$) and **(b)** $x = 0.40$ ($n = 2$) sample. **c, d** Schematic of the **(c)** 1D and **(d)** 2D Dirac fermion along the S - X - S direction (k_y). **e** The energy contour near Fermi energy (E_F) of the k_x - k_y plane with theoretical BZ appended (black solid lines). **f, g** The spectrum **(f)** along $\bar{\Gamma} - \bar{X} - \bar{\Gamma}$ and the spectrum **(g)** at $k_y = -0.30 \text{ \AA}^{-1}$ (orange dashed lines) with linear fitting result of the Dirac fermion appended for $x = 0.43$ sample. **h-j** Same as **e-g**, but for $x = 0.40$ sample. Data in Fig. 3e-j were collected at $h\nu = 56 \text{ eV}$.

see the Dirac fermion velocity exhibits a periodic variation from \bar{X} to \bar{S} with a difference ($\frac{V_{\max} - V_{\min}}{V_{\max}}$) of $\sim 55.1\%$ for $x = 0.40$ ($n = 2$) sample. Meanwhile, there is much smaller variation ($\sim 17.7\%$) in the Dirac velocity for $x = 0.43$ ($n = 3$) sample, demonstrating the dimension-crossover.

Such behavior could be captured by the following simple model (detailed description could be found in Supplementary Discussion). The two low-energy bands that form the Dirac nodal line are mainly contributed from orbitals at Nb sites in the NbTe_2 chains. We first construct a model for a single chain. As illustrated in Fig. 4b, the unit cell of the zigzag-shaped chain contains two sites A and B (which may be thought of as corresponding to the Nb sites, although such a correspondence is not necessary). Putting one active orbital per site and denoting the hopping strength between neighboring sites by t , the single-chain model takes the form of

$$\mathcal{H}_{\text{Chain}} = \begin{bmatrix} 0 & t(1 + e^{-ik_x a}) \\ t(1 + e^{ik_x a}) & 0 \end{bmatrix}, \quad (1)$$

where we assume the chain is orientated along the x direction with a lattice constant a . This single chain model looks similar to the famous SSH model. However, there is a crucial distinction: the system here has an important constraint from the glide mirror symmetry \tilde{M}_y . As indicated in Fig. 4d, \tilde{M}_y requires that the sites A and B must be equivalent and the hopping strengths between all neighboring sites must be the same. The algebraic relation $(T\tilde{M}_y)^2 = -1$ for $k_x a = \pi$ further dictates that the bands must form Kramers like degeneracy at the BZ (Fig. 4e) boundary. In our single-chain model (1), we have

$$\tilde{M}_y = \begin{bmatrix} 0 & e^{-ik_x a} \\ 1 & 0 \end{bmatrix}, \quad (2)$$

and the spectrum $E = \pm 2t \cos(\frac{k_x a}{2})$ is gapless with a 1D Dirac type crossing at $k_x a = \pi$ (Fig. 4f). This is in contrast with the conventional SSH model, where dimerization is allowed due to the lack of this glide mirror symmetry and it makes the spectrum typically gapped. To highlight the distinction, we call the single-chain model (1) a Dirac SSH model. Next, we extend this Dirac SSH

model to 2D by forming an array of the chains. Denoting the lattice period along the y direction (inter-chain distance) by b and including the inter-chain coupling t' , as illustrated in Fig. 4c, our 2D Dirac SSH model can be expressed as $\mathcal{H}_{2D} = \mathcal{H}_{\text{chain}} + \mathcal{H}_{\text{inter}}$ with the inter-chain coupling

$$\mathcal{H}_{\text{inter}} = \begin{bmatrix} 0 & t'e^{-iky b}(1 + e^{-ik_x a}) \\ t'e^{iky b}(1 + e^{ik_x a}) & 0 \end{bmatrix}. \quad (3)$$

Importantly, the inter-chain coupling cannot open a gap in the Dirac spectrum. Because \tilde{M}_y is still preserved, no matter how big t' is, the 2D model always has a symmetry enforced Dirac nodal line at the BZ boundary $k_x a = \pi$. Nevertheless, the inter-chain coupling does change the dispersion around the nodal line. The spectrum of our 2D model can be readily found to be

$$E = \pm 2 \cos \frac{k_x a}{2} \sqrt{t^2 + 2tt' \cos k_y b + t'^2}. \quad (4)$$

Then the Fermi velocity around the Dirac line in the k_x direction is given by

$$V_f|_{k_x a = \pm \pi} = \pm \frac{a}{\hbar} \sqrt{t^2 + 2tt' \cos k_y b + t'^2}, \quad (5)$$

which depends on k_y when t' is nonzero (Fig. 4g). Apparently, the magnitude of the velocity varies along the nodal line, as illustrated in Fig. 4h, in an interval $[|t| - |t'|] \frac{a}{\hbar}, [|t| + |t'|] \frac{a}{\hbar}$ (see Supplementary Figs. 6–10 for more details of the models). This captures the qualitative features observed in our experiment. The discussion shows that our proposed Dirac SSH model offers a good starting point for understanding the physics in NbSi_xTe_2 and for studying general dimension-crossover of Dirac fermions.

DISCUSSION

In summary, we systematically investigated the electronic structure of the composition-tunable layered compounds NbSi_xTe_2 ($x = 0.40$ and 0.43) and confirmed the 1D Dirac fermion originated from the NbTe_2 chains on the surface in the NbSi_xTe_2 ($x = 0.43$) system. Dirac nodal line structure protected by the combined \tilde{M}_y and time-reversal symmetry T proves the NbSi_xTe_2

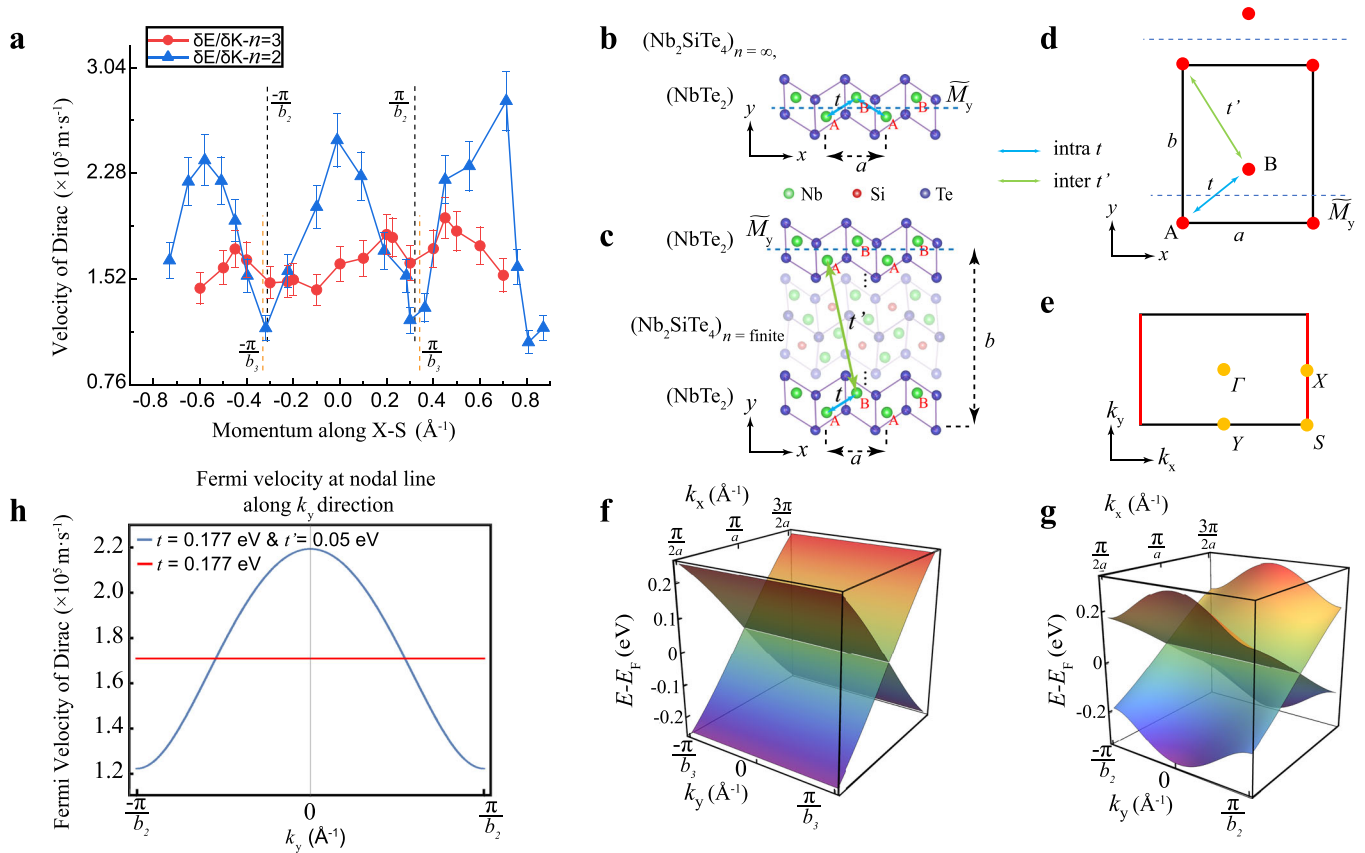


Fig. 4 Dimension-crossover and the Dirac SSH model of the Dirac fermion. **a** The extracted Dirac fermion velocity along X - S in NbSi_xTe_2 for $x = 0.43$ ($n = 3$) and $x = 0.40$ ($n = 2$) samples with the theoretical BZ period appended. **b** Schematic of a single NbTe_2 chain. Sites A , B and intra-chain coupling t as well as glide mirror \tilde{M}_y are labeled. **c** Schematic of the NbTe_2 chains array extracted from the NbSi_xTe_2 surface. NbTe_2 chain distance along the y direction is marked by b , intra-chain coupling (t) and inter-chain coupling (t') are labeled. **d** Plot of the extracted Dirac SSH model from Fig. 4c. Two sites A and B are included in the cell, related by glide mirror \tilde{M}_y . The lattice constants, the intra- and interchain hopping t and t' are labeled. The dash line denotes the glide plane. **e** Corresponding BZ for the Dirac SSH model. The orange points denote the high symmetry points and red lines denote the location of nodal line at $k_x a = \pm\pi$. **f** 1D Dirac SSH model derived dispersion with $t = 0.177$ eV. **g** 2D Dirac SSH model derived dispersion with $t = 0.177$ eV and $t' = 0.05$ eV. **h** Calculated Fermi velocity of the Dirac fermion along the k_x direction and its evolution along the k_y direction with $t = 0.177$ eV (red curve) and $t = 0.177$ eV, $t' = 0.05$ eV (blue curve).

system as a topological semimetal which is consistent with the ab-initio calculations. The interaction between NbTe_2 chains increases as x decreases, and Dirac fermion goes through a dimension-crossover from 1D to 2D which can be explained by a Dirac SSH model. A tunable and unidirectional 1D Dirac electron system is demonstrated in our experiment, which offers a versatile platform for the exploration of intriguing 1D physics and device applications.

METHODS

Sample preparation

High-quality NbSi_xTe_2 ($x = 0.33$ to 0.5) single crystals were grown by the chemical vapor transport method by using iodine (I_2) as the transport agent. For crystal growth, the polycrystalline powders were synthesized by the direct solid-state reaction using the stoichiometric mixture of high-purity Nb (Alfa Aesar 99.99%), Si (Alfa Aesar 99.999%), and Te powder (Alfa Aesar 99.999%) as starting materials. The ground mixture was sealed in a quartz tube under high vacuum, put in a box furnace, and subsequently heated at 900°C for several days to prepare the polycrystalline samples. Then the obtained powder and high-purity I_2 (Alfa Aesar, 99.9985%) powder were mixed, ground, sealed in another evacuated quartz tube, and placed in a double-zone furnace. The temperature profile in the furnace

was set to be 850°C (growth side) – 950°C (source side) to grow crystals. After kept this temperature difference for over 10 days, the sheet-like crystals with metallic luster were obtained.

Angle-resolved photoemission spectroscopy

Synchrotron-based ARPES measurements were performed at the Beamline 10.0.1 of the Advanced Light Source (ALS), Lawrence Berkeley National Laboratory. The samples were cleaved in situ and measurements were performed with the temperature of 20 K under UHV below 3×10^{-11} Torr. Data were collected by a Scienta R4000 analyzer. The total energy and angle resolutions were 10 meV and 0.2° , respectively.

DATA AVAILABILITY

The data that support the findings of this study are available from the corresponding authors upon request. Database for material sciences hosted at Institute of Physics and Computer Network Information Center, Chinese Academy of Sciences contains the crystallographic data of this work. These data can be obtained free of charge via <http://materiae.iphys.ac.cn/materials/MAT00003867> and <http://materiae.iphys.ac.cn/materials/MAT00010455>.

Received: 24 December 2021; Accepted: 22 April 2022;
Published online: 24 May 2022

REFERENCES

- Alidoust, N. et al. Observation of monolayer valence band spin-orbit effect and induced quantum well states in MoX_2 . *Nat. Commun.* **5**, 4673 (2014).
- Das, S., Chen, H. Y., Penumatcha, A. V. & Appenzeller, J. High performance multilayer MoS_2 transistors with scandium contacts. *Nano Lett.* **13**, 100–105 (2013).
- Gong, C. et al. Discovery of intrinsic ferromagnetism in two-dimensional van der Waals crystals. *Nature* **546**, 265–269 (2017).
- Liu, H. et al. Phosphorene: an unexplored 2D semiconductor with a high hole mobility. *ACS Nano* **8**, 4033–4041 (2014).
- Marchiori, E. et al. Nanoscale magnetic field imaging for 2D materials. *Nat. Rev. Phys.* **4**, 49–60 (2021).
- Qian, X., Liu, J., Fu, L. & Li, J. Quantum spin Hall effect in two-dimensional transition metal dichalcogenides. *Science* **346**, 1344–1347 (2014).
- Wang, Z. et al. Very large tunneling magnetoresistance in layered magnetic semiconductor CrI_3 . *Nat. Commun.* **9**, 2516 (2018).
- Chen, C. et al. Robustness of topological order and formation of quantum well states in topological insulators exposed to ambient environment. *Proc. Natl Acad. Sci. USA* **109**, 3694–3698 (2012).
- Zhang, J. et al. Direct visualization and manipulation of tunable quantum well state in semiconducting Nb_2SiTe_4 . *ACS Nano* **15**, 15850–15857 (2021).
- Chen, Y. L. et al. Experimental realization of a three-dimensional topological insulator, Bi_2Te_3 . *Science* **325**, 178–181 (2009).
- Fu, L., Kane, C. L. & Mele, E. J. Topological insulators in three dimensions. *Phys. Rev. Lett.* **98**, 106803 (2007).
- Zhang, H. et al. Topological insulators in Bi_2Se_3 , Bi_2Te_3 and Sb_2Te_3 with a single Dirac cone on the surface. *Nat. Phys.* **5**, 438–442 (2009).
- Zhang, Y. et al. Crossover of the three-dimensional topological insulator Bi_2Se_3 to the two-dimensional limit. *Nat. Phys.* **6**, 584–588 (2010).
- Reyren, N. et al. Superconducting interfaces between insulating oxides. *Science* **317**, 1196–1199 (2007).
- Ohtomo, A. & Hwang, H. Y. A high-mobility electron gas at the $\text{LaAlO}_3/\text{SrTiO}_3$ heterointerface. *Nature* **427**, 423–426 (2004).
- Caviglia, A. D. et al. Electric field control of the $\text{LaAlO}_3/\text{SrTiO}_3$ interface ground state. *Nature* **456**, 624–627 (2008).
- Yu, Y. et al. Gate-tunable phase transitions in thin flakes of 1T-Ta S_2 . *Nat. Nanotechnol.* **10**, 270–276 (2015).
- Xi, X. et al. Strongly enhanced charge-density-wave order in monolayer NbSe_2 . *Nat. Nanotechnol.* **10**, 765–769 (2015).
- Ugeda, M. M. et al. Characterization of collective ground states in single-layer NbSe_2 . *Nat. Phys.* **12**, 92–97 (2016).
- Sipos, B. et al. From Mott state to superconductivity in 1T-Ta S_2 . *Nat. Mater.* **7**, 960–965 (2008).
- Luo, S., He, L. & Li, M. Spin-momentum locked interaction between guided photons and surface electrons in topological insulators. *Nat. Commun.* **8**, 2141 (2017).
- Li, P. et al. Spin-momentum locking and spin-orbit torques in magnetic nano-heterojunctions composed of Weyl semimetal WTe_2 . *Nat. Commun.* **9**, 3990 (2018).
- Wang, Z. et al. Anisotropic two-dimensional electron gas at SrTiO_3 (110). *Proc. Natl Acad. Sci. USA* **111**, 3933–3937 (2014).
- Burch, K. S., Mandrus, D. & Park, J.-G. Magnetism in two-dimensional van der Waals materials. *Nature* **563**, 47–52 (2018).
- Fei, Z. et al. Two-dimensional itinerant ferromagnetism in atomically thin Fe_3GeTe_2 . *Nat. Mater.* **17**, 778–782 (2018).
- Peierls, R. E. Quantum theory of solids. *Int. Ser. Monogr. Phys.* <https://zbmath.org/1089.81002> (1955).
- Kagoshima, S. Peierls phase transition. *Jpn J. Appl. Phys.* **20**, 1617–1634 (1981).
- Su, W. P., Schrieffer, J. R. & Heeger, A. J. Solitons in polyacetylene. *Phys. Rev. Lett.* **42**, 1698–1701 (1979).
- Heeger, A. J., Kivelson, S., Schrieffer, J. R. & Su, W. P. Solitons in conducting polymers. *Rev. Mod. Phys.* **60**, 781–850 (1988).
- Jackiw, R. & Rebbi, C. Solitons with fermion number 1/2. *Phys. Rev. D.* **13**, 3398–3409 (1976).
- Meier, E. J., An, F. A. & Gadway, B. Observation of the topological soliton state in the Su–Schrieffer–Heeger model. *Nat. Commun.* **7**, 13986 (2016).
- Xiao, L. et al. Observation of topological edge states in parity–time–symmetric quantum walks. *Nat. Phys.* **13**, 1117–1123 (2017).
- Hafezi, M., Mittal, S., Fan, J., Migdall, A. & Taylor, J. M. Imaging topological edge states in silicon photonics. *Nat. Photon.* **7**, 1001–1005 (2013).
- Drozhdov, I. K. et al. One-dimensional topological edge states of bismuth bilayers. *Nat. Phys.* **10**, 664–669 (2014).
- Benalcazar, W. A., Bernevig, B. A. & Hughes, T. L. Electric multipole moments, topological multipole moment pumping, and chiral hinge states in crystalline insulators. *Phys. Rev. B* **96**, 245115 (2017).
- Schindler, F. et al. Higher-order topology in bismuth. *Nat. Phys.* **14**, 918–924 (2018).
- Kunst, F. K., van Miert, G. & Bergholtz, E. J. Lattice models with exactly solvable topological hinge and corner states. *Phys. Rev. B* **97**, 241405 (2018).
- Tomonaga, S.-I. Remarks on Bloch’s method of sound waves applied to many-fermion problems. *Prog. Theor. Phys.* **5**, 544–569 (1950).
- Luttinger, J. M. An exactly soluble model of a many-fermion system. *J. Math. Phys.* **4**, 1154–1162 (1963).
- Mattis, D. C. & Lieb, E. H. Exact solution of a many-fermion system and its associated boson field. *J. Math. Phys.* **6**, 304–312 (1965).
- Ahn, J. R. et al. Mechanism of gap opening in a triple-band Peierls system: in atomic wires on Si. *Phys. Rev. Lett.* **93**, 106401 (2004).
- Jin, G., Tang, Y. S., Liu, J. L. & Wang, K. L. Growth and study of self-organized Ge quantum wires on Si(111) substrates. *Appl. Phys. Lett.* **74**, 2471–2473 (1999).
- Kamins, T. I., Li, X., Williams, R. S. & Liu, X. Growth and structure of chemically vapor deposited Ge nanowires on Si substrates. *Nano Lett.* **4**, 503–506 (2004).
- Spurgeon, J. M. et al. Repeated epitaxial growth and transfer of arrays of patterned, vertically aligned, crystalline Si wires from a single Si(111) substrate. *Appl. Phys. Lett.* **93**, 032112 (2008).
- Salomon, D. et al. Metal organic vapour-phase epitaxy growth of GaN wires on Si(111) for light-emitting diode applications. *Nanoscale Res. Lett.* **8**, 61 (2013).
- Watanabe, T., Yamada, Y., Sakai, M., Sakai, S. & Yamauchi, Y. Pt- and Au-induced monodirectional nanowires on Ge(110). *Surf. Sci.* **653**, 71–75 (2016).
- Blumenstein, C. et al. Au-induced quantum chains on Ge(001)—symmetries, long-range order and the conduction path. *J. Phys. Condens. Matter* **25**, 014015 (2012).
- Zhou, J. et al. Large-area nanowire arrays of molybdenum and molybdenum oxides: synthesis and field emission properties. *Adv. Mater.* **15**, 1835–1840 (2003).
- Liang, R., Cao, H. & Qian, D. MoO_3 nanowires as electrochemical pseudocapacitor materials. *Chem. Commun.* **47**, 10305–10307 (2011).
- Wang, F. et al. New Luttinger–liquid physics from photoemission on $\text{Li}_{0.9}\text{Mo}_6\text{O}_{17}$. *Phys. Rev. Lett.* **96**, 196403 (2006).
- Yang, L. X. et al. Bypassing the structural bottleneck in the ultrafast melting of electronic order. *Phys. Rev. Lett.* **125**, 266402 (2020).
- Chen, C. et al. Observation of topological electronic structure in quasi-1d superconductor TaSe_3 . *Matter* **3**, 2055–2065 (2020).
- Stonemeyer, S. et al. Stabilization of NbTe_3 , VTe_3 , and TlTe_3 via nanotube encapsulation. *J. Am. Chem. Soc.* **143**, 4563–4568 (2021).
- Pham, T. et al. Torsional instability in the single-chain limit of a transition metal trichalcogenide. *Science* **361**, 263–266 (2018).
- Jiang, B. Y. et al. Tunable plasmonic reflection by bound 1D electron states in a 2D Dirac metal. *Phys. Rev. Lett.* **117**, 086801 (2016).
- Wang, X. F. et al. Tunable electronic anisotropy in single-crystal $\text{A}_2\text{Cr}_3\text{As}_3$ ($\text{A} = \text{K}, \text{Rb}$) quasi-one-dimensional superconductors. *Phys. Rev. B* **92**, 020508 (2015).
- Fan, Z.-Q., Jiang, X.-W., Wei, Z., Luo, J.-W. & Li, S.-S. Tunable electronic structures of GeSe nanosheets and nanoribbons. *J. Phys. Chem. C* **121**, 14373–14379 (2017).
- Wang, B. et al. One-dimensional metal embedded in two-dimensional semiconductor in $\text{Nb}_2\text{Si}_{x-1}\text{Te}_4$. *ACS Nano* **15**, 7149–7154 (2021).
- Boucher, F., Zhukov, V. & Evain, M. MA_xTe_2 phases ($\text{M} = \text{Nb}, \text{Ta}$; $\text{A} = \text{Si}, \text{Ge}$; $1/3 \leq x \leq 1/2$): an electronic band structure calculation analysis. *Inorg. Chem.* **35**, 7649–7654 (1996).
- Yang, T. Y. et al. Directional massless Dirac fermions in a layered van der Waals material with one-dimensional long-range order. *Nat. Mater.* **19**, 27–33 (2020).
- Li, S. et al. Nonsymmetrical-symmetry-protected hourglass Dirac loop, nodal line, and Dirac point in bulk and monolayer X_3SiTe_6 ($\text{X} = \text{Ta}, \text{Nb}$). *Phys. Rev. B* **97**, 045131 (2018).
- Sato, T. et al. Observation of band crossings protected by nonsymmetrical symmetry in the layered ternary telluride Ta_3SiTe_6 . *Phys. Rev. B* **98**, 121111 (2018).
- Zhu, Z. et al. A tunable and unidirectional one-dimensional electronic system $\text{Nb}_{2n+1}\text{Si}_n\text{Te}_{4n+2}$. *npj Quant. Mater.* **5**, 35 (2020).

ACKNOWLEDGEMENTS

We thank W. Li, F. Yang and L. Zhang for the helpful discussion. We acknowledge the financial support from the National Key R&D program of China (Grants No.2017YFA0305400), the National Natural Science Foundation of China (No. 51902152) and Singapore MOE AcRF Tier 2 (MOE-T2EP50220-0011). This research used resources of the Advanced Light Source, a U.S. DOE Office of Science User Facility under contract No. DE-AC02-05CH11231.

AUTHOR CONTRIBUTIONS

Z.L. and Yulin Chen supervised the project. J.Z. performed the ARPES measurement with the help of A.L., S.-K.M., and C.C. S.A.Y. and X.F. provided the theoretical

modeling support. Y.L. and Yanbin Chen synthesized the crystals. All authors discussed the results and contributed to the paper.

COMPETING INTERESTS

The authors declare no competing interests.

ADDITIONAL INFORMATION

Supplementary information The online version contains supplementary material available at <https://doi.org/10.1038/s41535-022-00462-6>.

Correspondence and requests for materials should be addressed to Yulin Chen or Zhongkai Liu.

Reprints and permission information is available at <http://www.nature.com/reprints>

Publisher's note Springer Nature remains neutral with regard to jurisdictional claims in published maps and institutional affiliations.



Open Access This article is licensed under a Creative Commons Attribution 4.0 International License, which permits use, sharing, adaptation, distribution and reproduction in any medium or format, as long as you give appropriate credit to the original author(s) and the source, provide a link to the Creative Commons license, and indicate if changes were made. The images or other third party material in this article are included in the article's Creative Commons license, unless indicated otherwise in a credit line to the material. If material is not included in the article's Creative Commons license and your intended use is not permitted by statutory regulation or exceeds the permitted use, you will need to obtain permission directly from the copyright holder. To view a copy of this license, visit <http://creativecommons.org/licenses/by/4.0/>.

© The Author(s) 2022